V European Conference on Computational Fluid Dynamics
ECCOMAS CFD 2010
J. C. F. Pereira and A. Sequeira (Eds)
Lisbon, Portugal,14-17 June 2010

# EFFICIENCY INVESTIGATION OF A PARALLEL HIERARCHICAL GRID BASED AEROACOUSTIC CODE FOR LOW MACH NUMBERS AND COMPLEX GEOMETRIES

**Michael Kornhaas, Dörte C. Sternel and Michael Schäfer**

Technische Universität Darmstadt, Institute of Numerical Methods in Mechanical Engineering,
Dolivostraße 15, 64293 Darmstadt, Germany,
e-mail: kornhaas@fnb.tu-darmstadt.de

**Key words:** Computational Aero-Acoustics, Linearized Euler Equations, Large Eddy Simulation, Hierarchical Grids, Efficiency

**Abstract.** *We present a numerical scheme for the simulation of aeroacoustic noise, caused by flows at low Mach numbers, within and/or around complex geometries. To speed up the coupled simulations and to account for the different length scales of small turbulence structures and long-wave acoustics, the acoustic field can be computed on the hierarchically coarsened computational fluid dynamics (CFD) grid. Further, multiple acoustic time steps can be performed within one CFD time step.*
*To evaluate the numerical and parallel efficiency of the method, numerical simulations of a generic acoustic test case are presented. The efficiency of the hierarchical grid approach for aeroacoustics is investigated on the basis of simulations of an aeroacoustic test case with different grids for the acoustic part of the simulation.*

## 1 INTRODUCTION

A major part of the noise generation in urban environments is caused by turbulent flows, e.g., the noise of driving cars, fans, etc. Even though the prediction and reduction of noise is of great importance and an important issue during the design process, the physical mechanisms of noise generation in turbulent flows are still not fully understood for many applications. Computational fluid dynamics (CFD), especially time resolved methods like the Direct Numerical Simulation (DNS) and the Large Eddy Simulation (LES) can be a powerful tool for a better understanding of flow physics and the mechanisms of aerodynamic noise generation. This is not only because of their capability of predicting fluctuating quantities that can be used as source terms for computational aeroacoustics (CAA) simulations, but also because of their higher accuracy compared to the numerically cheaper Reynolds Averaged Navier-Stokes (RANS) simulations. However, only recently sufficient computational power has become available to perform such computations for configurations of practical interest.
We present a numerical scheme for the simulation of aerodynamic noise caused by flows at low Mach numbers within and/or around complex geometries.
To account for sound propagation the in-house finite-volume flow solver FASTEST [1] is extended by a fully parallelized high resolution (HR) finite-volume (FV) scheme that solves the linearized Euler equations (LEE) on boundary fitted, block-structured hexahedral meshes. Aeroacoustic sources are obtained from the unsteady calculated flow field following the basic ideas of Hardin's and Pope's acoustic/viscous splitting technique [2].
In order to speed up the coupled simulation and to account for the very different length scales of small turbulence structures and the long-wave acoustics, the acoustic field is computed on the hierarchically coarsened CFD grid. Further, different time scales are employed so that multiple acoustic time steps can be performed within one CFD time step.
In order to prove the efficiency and accuracy of the presented method, numerical simulations of a generic acoustic test case are carried out to investigate the scalability of the implemented scheme with respect to the problem size and the parallelization.
Further, the influence of the hierarchically coarsened acoustic mesh on the computational time and the quality of the results is studied for an aeroacoustic test case.

## 2 NUMERICAL METHOD

### 2.1 The Flow Solver FASTEST

The incompressible fully parallelized in-house FV solver FASTEST [1] solves the *Navier-Stokes* equations on boundary fitted, block structured hexahedral grids. Convective and diffusive fluxes are approximated with a second-order central difference scheme.
To account for turbulence different RANS models and LES subgrid models are implemented. The implicit second-order Crank-Nicholson scheme is applied for time discretization. Pressure velocity coupling is realized with the SIMPLE algorithm that serves as

smoother in a geometric multigrid scheme with standard restriction and prolongation [3]. The resulting linear systems of equations are solved with an ILU method.

### 2.2 Modeling of Aeroacoustic Sources and Sound Propagation

Time resolved computations of the flow field like LES allow the calculation of aeroacoustic source terms according to different aeroacoustic analogies like Lighthill's analogy [4] or Hardin and Pope's [2] acoustic/viscous splitting approach.
Following the basic ideas of the latter approach, the compressible flow field at low Mach numbers is assumed to be an incompressible hydrodynamic part (denoted with $*^{inc}$) and an acoustic fluctuation (denoted with $*'$). In the following $\vec{u} = (u, v, w)^T$ stands for the velocity vector, $p$ for the pressure, $\rho$ for the density and $\kappa$ for the adiabatic exponent. If viscous effects are neglected, this approach leads to a system of equations which is equivalent to the *Linearized Euler Equations* (LEE) on the left hand side and acoustic sources on the right hand side:

$$\frac{\partial \rho'}{\partial t} + \rho^{inc} \nabla \cdot \vec{u}' + \vec{u}^{inc} \cdot \nabla \rho' = 0 \tag{1}$$

$$\rho^{inc} \frac{\partial \vec{u}'}{\partial t} + \rho^{inc} \left( \vec{u}^{inc} \cdot \nabla \right) \vec{u}' + \nabla p' = 0 \tag{2}$$

$$\frac{\partial p'}{\partial t} + \kappa p^{inc} \nabla \cdot \vec{u}' + \vec{u}^{inc} \cdot \nabla p' = -\frac{\partial p^{inc}}{\partial t} - \vec{u}^{inc} \cdot \nabla p^{inc} \tag{3}$$

### 2.3 High Resolution Finite Volume Scheme for Linearized Euler Equations

To account for sound propagation a FV solver for the LEE is implemented in the flow solver FASTEST [1]. The numerical solution method will be outlined briefly in the following. More detailed information about the applied techniques can be found in [5] or [6]. The LEE can be rewritten in their flux formulation with the variable vector $\vec{U}$, the fluxes $\vec{F}$, $\vec{G}$ and $\vec{H}$ and the aeroacoustic sources $\vec{Q}$:

$$\frac{\partial}{\partial t} \underbrace{\begin{bmatrix} \rho' \\ u' \\ v' \\ w' \\ p' \end{bmatrix}}_{\vec{U}} + \frac{\partial}{\partial x} \underbrace{\begin{bmatrix} u^{inc}\rho' + \rho^{inc}u' \\ u^{inc}u' + \frac{p'}{\rho^{inc}} \\ u^{inc}v' \\ u^{inc}w' \\ u^{inc}p' + \kappa p^{inc}u' \end{bmatrix}}_{\vec{F}} + \frac{\partial}{\partial y} \underbrace{\begin{bmatrix} v^{inc}\rho' + \rho^{inc}v' \\ v^{inc}u' \\ v^{inc}u' + \frac{p'}{\rho^{inc}} \\ v^{inc}w' \\ v^{inc}p' + \kappa p^{inc}v' \end{bmatrix}}_{\vec{G}} + \frac{\partial}{\partial z} \underbrace{\begin{bmatrix} w^{inc}\rho' + \rho^{inc}w' \\ w^{inc}u' \\ w^{inc}v' \\ w^{inc}w' + \frac{p'}{\rho^{inc}} \\ w^{inc}p' + \kappa p^{inc}w' \end{bmatrix}}_{\vec{H}} = \underbrace{\begin{bmatrix} Q_{\rho'} \\ Q_{u'} \\ Q_{v'} \\ Q_{w'} \\ Q_{p'} \end{bmatrix}}_{\vec{Q}} \tag{4}$$

Applying the chain rule to the flux formulation (4) leads to

$$\begin{aligned}
&\frac{\partial}{\partial t}\begin{bmatrix}\rho'\\u'\\v'\\w'\\p'\end{bmatrix}+\underbrace{\begin{bmatrix}u^{inc}&\rho^{inc}&0&0&0\\0&u^{inc}&0&0&1/\rho^{inc}\\0&0&u^{inc}&0&0\\0&0&0&u^{inc}&0\\0&\rho^{inc}c^2&0&0&u^{inc}\end{bmatrix}}_{\mathbf{A}}\frac{\partial}{\partial x}\begin{bmatrix}\rho'\\u'\\v'\\w'\\p'\end{bmatrix}\\
&+\underbrace{\begin{bmatrix}v^{inc}&0&\rho^{inc}&0&0\\0&v^{inc}&0&0&0\\0&0&v^{inc}&0&1/\rho^{inc}\\0&0&0&v^{inc}&0\\0&0&\rho^{inc}c^2&0&v^{inc}\end{bmatrix}}_{\mathbf{B}}\frac{\partial}{\partial y}\begin{bmatrix}\rho'\\u'\\v'\\w'\\p'\end{bmatrix}+\\
&\underbrace{\begin{bmatrix}w^{inc}&0&0&\rho^{inc}&0\\0&w^{inc}&0&0&0\\0&0&w^{inc}&0&0\\0&0&0&w^{inc}&1/\rho^{inc}\\0&0&0&\rho^{inc}c^2&w^{inc}\end{bmatrix}}_{\mathbf{C}}\frac{\partial}{\partial z}\begin{bmatrix}\rho'\\u'\\v'\\w'\\p'\end{bmatrix}=\begin{bmatrix}Q_{\rho'}\\Q_{u'}\\Q_{v'}\\Q_{w'}\\Q_{p'}\end{bmatrix}
\end{aligned}\tag{5}$$

with the speed of sound $c$ and the Jacobian matrices $\mathbf{A}$, $\mathbf{B}$, and $\mathbf{C}$ of the fluxes $\vec{F}$, $\vec{G}$, and $\vec{H}$, respectively. Applying the finite-volume approach and transforming the LEE into control volume (CV) face normal direction $\vec{n}$, with the local coordinate $\vec{\xi}$, leads to one 1-dimensional Riemann problem for each cell face. A general hexahedral CV with neighboring points is depicted in figure 1 (a). The 3D compass notation is used and cell centers are denoted with capital letters and the cell face centers with lower case letters. Figure 1 (b) shows an east face of a control volume with face normal coordinate $\xi$ and the face normal component of the variable vector $\vec{U}_\xi$. Applying the mid point rule for all appearing integrals, the cell face normal fluxes $\vec{F}_c$ for the cell faces $c = e, w, s, n, t, b$ can be computed in cell normal coordinates according to equation (6). Written for an east cell face of the size $A_e$ we get

$$\vec{F}_e(\vec{U}_\xi) = \left[(1-\Phi(r_e))\vec{F}_e^{UPW} + \Phi(r_e)\vec{F}_e^{LW}(\vec{U}_\xi)\right] A_e \tag{6}$$

where $\vec{F}_c^{UPW}$ stands for the upwind flux with the matrix of the right eigenvectors $\mathbf{K}$ of Jacobian $\mathbf{A}_\xi$ of the cell face normal flux and the matrix of the eigenvalues $\mathbf{\Lambda} = diag\lambda_i$:

$$\vec{F}_e^{UPW}(\vec{U}_\xi) = \frac{1}{2}\mathbf{A}_\xi(\vec{U}_{E\xi}+\vec{U}_{P\xi}) - \frac{1}{2}\mathbf{K}|\mathbf{\Lambda}|\mathbf{K^{-1}}(\vec{U}_{P\xi}-\vec{U}_{E\xi}) \tag{7}$$

$\vec{F}_c^{\,LW}$ stands for the Lax-Wendroff flux with the acoustic time step size $\Delta t_{CAA}$ and the distance $\Delta x_\xi$ between the neighboring cell centers:

$$\vec{F}_e^{LW}(\vec{U}_\xi) = \frac{1}{2}\mathbf{A}_\xi(\vec{U}_{E\xi}+\vec{U}_{P\xi}) - \frac{\Delta t_{CAA}}{\Delta x_\xi}\mathbf{A}_\xi^2(\vec{U}_{P\xi}-\vec{U}_{E\xi}) \tag{8}$$

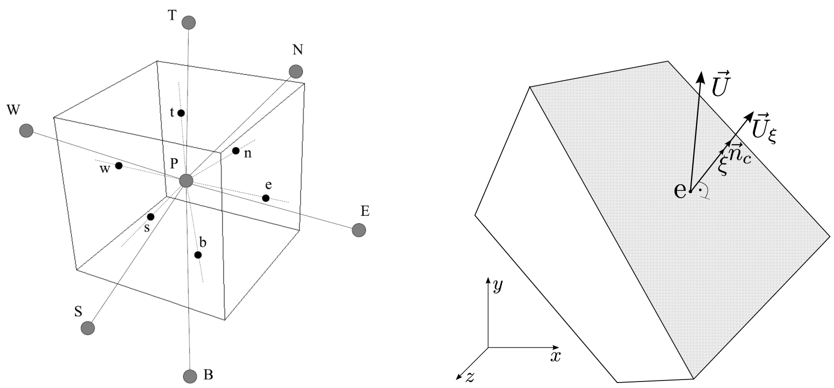


(a) Control Volume with neighboring points

(b) Cell face normal coordinates and transformed variable vector $\vec{U}_\xi$

Figure 1: Variable arrangement.

To make the scheme TVD (total variation diminishing) a flux limiter function $\Phi(r_c)$, e.g., Van Leers [7] monotonized central (MC) Limiter, is required

$$\phi_{MC}(r_c) = \max\left[0, \min\left(2r_c, 0.5(1 + r_c), 2\right)\right]; \quad \lim_{r_c \to \infty} \phi_{MC}(r_c) = 2 \tag{9}$$

where $r_c$ represents the ratio of successive gradients in the cell face local direction. Written for an east face we obtain

$$r_e = \frac{u_{iP} - u_{iW}}{u_{iE} - u_{iP}}; \quad \dot{m} \geq 0 \tag{10}$$

$$r_e = \frac{u_{iEE} - u_{iE}}{u_{iE} - u_{iP}}; \quad \dot{m} < 0 \tag{11}$$

depending on the upwind direction $\dot{m}$. Knowing the cell normal fluxes and applying a dimensional splitting scheme in the logical coordinates $i$, $j$, and $k$, the variable vector $\vec{U}^{(n+c/6)^*}$ can be updated for all six cell faces $c = 1, ..., 6$ according to

$$\vec{U}^{(n+c/6)^*} = \vec{U}^{(n+(c-1)/6)^*} - \frac{\Delta t_{CAA}}{V} \vec{F}_{c,xyz}(\vec{U}^n) \tag{12}$$

with the volume $V$ of the CV and the cell face normal flux $\vec{F}_{c,xyz}$ transformed back to Cartesian coordinates. After all six CV faces have been considered the aeroacoustic sources can be included to obtain the new time level $n + 1$:

$$\vec{U}^{n+1} = \vec{U}^{(n+1)^*} + \Delta t_{CAA} \vec{Q} \tag{13}$$

The outlined method allows a highly efficient implementation at minimal memory requirements since the fluxes do not need to be stored and the routine for the flux calculation has to be run only once for each of the three index directions (if neighboring nodes are considered). The described FV scheme is fully parallelized using the message passing interface MPI.

### 2.4 Acceleration of the Coupled Simulation

Since time and length scales between acoustic waves spreading with the speed of sound and small scale turbulence structures are very different, especially at very low Mach numbers, an efficient computation in the time domain is a challenge. In the following we briefly outline the applied methods that are used to speed up the coupled simulation.

#### 2.4.1 Frozen Fluid Approach

For low Mach number flows the speed of sound $c$ is much larger than the speed of the flow. Using the time step size, that results from the maximum time step size suitable for the explicit FV acoustic solver, the computation of the incompressible flow field would be very inefficient, since the time step would be unnecessarily small.
For this reason we apply an uneven time coupling or "frozen fluid approach", so that only at each $N$th acoustic time step the aeroacoustic source terms are updated and $N$ acoustic time steps of the size $\Delta t_{CAA}$ are performed within a single CFD time step of the size $\Delta t_{CFD}$ and

$$N = \frac{\Delta t_{CFD}}{\Delta t_{CAA}}. \tag{14}$$

If different grids for CFD and CAA are used as described in the following section, additionally an interpolation of the aeroacoustic sources to the CAA grid is required. This procedure is depicted in figure 2.

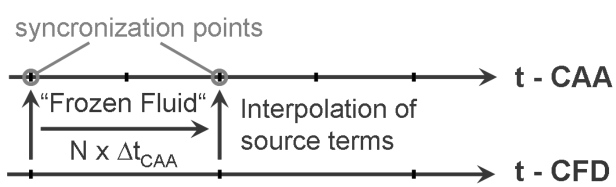


Figure 2: Frozen fluid approach - uneven time stepping within CFD and CAA solver.

#### 2.4.2 Hierarchical Grids for Acoustic Computation

Beside the very different time scales of an incompressible flow at low Mach number and the acoustics, the length scales of small turbulent eddies and the long scale acoustic waves are very different. This means that the acoustics may be over-resolved on the CFD mesh especially for situations where acoustic and flow domains are identical, such as for duct acoustics or the interior of a car. Therefore, for many applications it can be beneficial to calculate the acoustic quantities on the hierarchically coarsened CFD grid.
For this reason the multigrid functionality of FASTEST [1] is utilized to generate hierarchically coarsened grids for the acoustic simulation. In the 3D case the 1 times coarsened CFD grid has 8 times less control volumes. Further a 2 times greater acoustic time step

$\Delta t_{CAA}$ can be used. This means that the acoustic part of the coupled simulation is theoretically speed up by a factor of 16 if the CAA grid is the 1 times coarsened CFD grid, or even more, if even coarser grids are used. Applying such an approach the aeroacoustic sources are calculated on the fine CFD grid and are then interpolated on the CAA grid using a conservative multi-linear interpolation. This procedure is illustrated in figure 3.

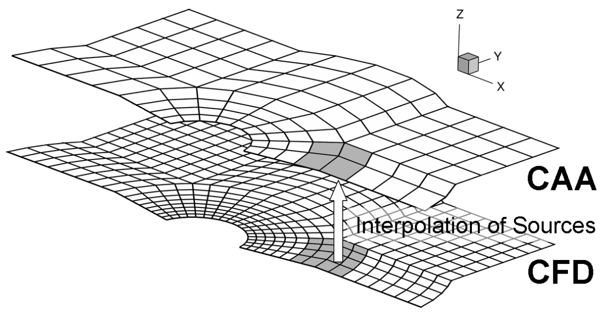


Figure 3: Hierarchical grid based CFD-CAA method. Interpolation of aeroacoustic source terms to the hierarchically coarsened CFD grid.

## 3 TEST CASES AND NUMERICAL SETUPS

Two test cases will be considered in this study. A pressure pulse as generic acoustic test case (section 3.1) to evaluate the numerical scalability and the parallel efficiency of the implemented FV method outlined in section 2.3.
To study the efficiency of the hierarchical grid scheme described in section 2.4.2 and its influence on the quality of the results, the aeroacoustic test case "plate in the turbulent wake of a circular cylinder" (section 3.2) is investigated.

### 3.1 Pressure Pulse

This generic test case consists of a unit cube ($1m \times 1m \times 1m$) with non reflecting boundary conditions at all boundaries. The problem domain is discretized with a single block that can be split for domain decomposition when performing parallel computations for the evaluation of the parallel efficiency of the method (see section 4.2). The numerical grid is equidistant in all directions. The number of CVs can be reduced by coarsening the finest discretization with more than $16 \times 10^6$ CVs. The fluid properties are summarized in table 1. The test case is designed as an initial value problem with:

$$p'_{t=0} = \begin{cases} 5Pa, & 0.4m \leq x_i \leq 0.6m \\ 0Pa, & rest \end{cases} \tag{15}$$

### 3.2 Plate in the Turbulent Wake of a Circular Cylinder

This aeroacoustic test case consists of a steel plate which is located in the turbulent wake of a circular cylinder (compare figure 4). The Reynolds number based on the diameter $D$ of the cylinder and the free stream velocity is around $Re_D = 2000$. To give

| | |
|---|---|
| fluid density $\rho$ $[kg/m^3]$ | 1.225 |
| hydrostatic pressure $p$ $[Pa]$ | 100000 |
| speed of sound $c$ $[m/s]$ | 347 |
| kinematic viscosity $\mu$ $[kg/(m\ s)]$ | $1.8 \times 10^{-5}$ |

Table 1: Fluid properties.

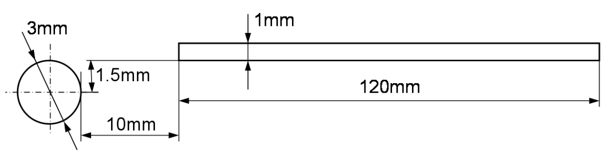


Figure 4: Test Case: Plate in the turbulent wake of a circular cylinder.

an impression of the turbulent structures around the test case, the $x$-component of the vorticity vector is shown in figure 5. The interaction of the vortex shedding at the cylinder with the front edge of the plate leads to high time dependent pressure fluctuations and therefore high aeroacoustic sources. Experimental investigations and numerical studies (Kornhaas et al. [8]) show a significant increase of the sound pressure level compared to a single cylinder. This makes the test case very interesting as validation case for low Mach number aeroacoustics.
The computational domain is of the size $1088mm \times 940mm \times 15mm$ and the CFD grid consists of $6.32 \times 10^6$ CVs. The simulations are carried out with 16 CPUs and a load balancing efficiency of 95.84%. The boundary layer around the cylinder is fully resolved whereas the boundary layer around the plate is not resolved. All walls are no slip walls for the flow and sonically hard walls for the acoustics. In spanwise direction periodic boundary conditions are applied. All other boundaries are non reflecting for acoustics and inlet respectively outlet boundaries for the flow.
LES are performed using the Smagorinsky model with the dynamic approach of Germano [9]. The fluid properties are the same as for the pressure pulse denoted in table 1. The grid structure in the vicinity of cylinder and plate in depicted in figure 5.

## 4 RESULTS

### 4.1 Numerical Efficiency and Scalability

To prove the efficient implementation of the acoustic solver, computations of the pressure pulse described in section 3.1 are carried out for different domain sizes on a single IBM Power6 CPU (4.7 GHz). The domain sizes and corresponding computing times for 100 acoustic time steps are summarized in table 2. The acoustic Courant number is approximately 0.4 for the finest grid. The time step size is kept constant for the simulations with the coarser grids. Figure 6 illustrates the computational time over the number of

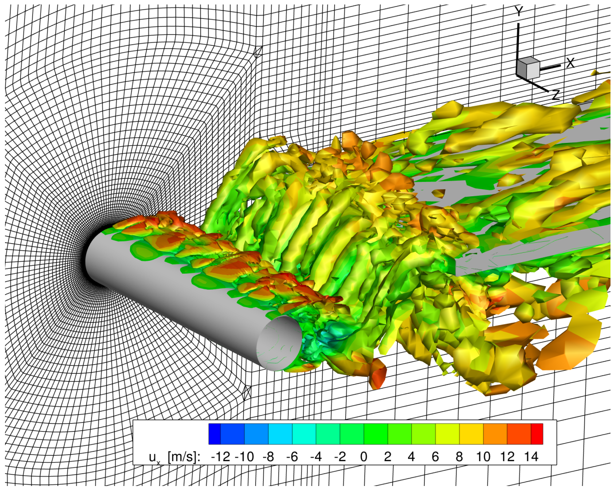


Figure 5: Vortical structures in the vicinity of the test case. $x$-component of the vorticity vector colored by the velocity component $u_x$ in $x$-direction and numerical grid (each second grid line is shown).

| # CV | 512 | 4096 | 32768 | 262144 | $2.09 \times 10^6$ | $4.19 \times 10^6$ | $8.38 \times 10^6$ | $16.77 \times 10^6$ |
|---|---|---|---|---|---|---|---|---|
| comp. time [s] | 0.025 | 0.197 | 1.588 | 13 | 111 | 230 | 447 | 914 |

Table 2: Numerical scalability. Computing time depending on domain size.

control volumes. The code shows a almost perfect linear scalability for the considered range of control volumes from 512 CVs up to more than $16 \times 10^6$ CVs.

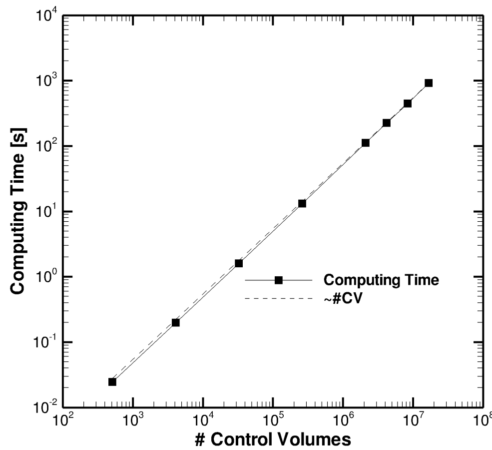


Figure 6: Computational time over number of CVs.

## 4.2 Parallel Efficiency

To evaluate the parallel efficiency and scalability of the implemented method, two numerical setups of the pressure pulse with $256^3$ CVs and $128^3$ CVs ($> 16 \times 10^6$ respectively

$\approx 2 \times 10^6$ CV) with different processor numbers up to 128 CPUs are performed. The computational domain is split into $P$ domains for $P$ CPUs with the same number of CV to obtain a load balancing of 100%. Further, it is taken care to minimize the interface sizes for more than 2 CPUs as shown in figure 7 for optimal communication between the processors. Again 100 acoustic time steps are calculated with an acoustic Courant number of approximately 0.4. Computing times, parallel speedup and the parallel efficiency are

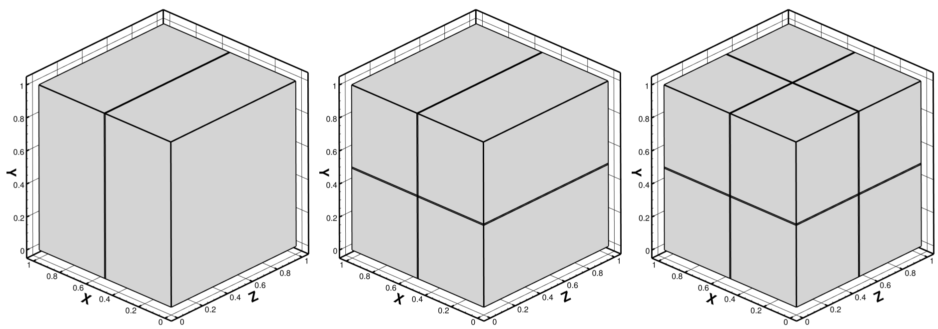

(a) 2 CPUs (b) 4 CPUs (c) 8 CPUs

Figure 7: Domain decomposition with respect to efficient communication.

evaluated for the performed simulations. The parallel speedup $S_P$ is defined as the ratio of the computing times obtained for one processor $t_{1CPU}$ and for $P$ CPUs $t_{PCPUs}$:

$$S_P = \frac{t_{1CPU}}{t_{PCPUs}} \tag{16}$$

Further we define an alternative parallel speedup $S_P^*$ for more than 2 CPUs with the reference computing time $t_{2CPUs}$ obtained for 2 CPUs:

$$S_P^* = \frac{2 \cdot t_{2CPUs}}{t_{PCPUs}}; \quad P \geq 2 \tag{17}$$

This allows to partly account for the communication latencies that may play a role for parallel computations if they are communication intense. The parallel efficiency $E_P$ is defined as:

$$E_P = \frac{t_{1CPU}}{P \cdot t_{PCPUs}} \tag{18}$$

Analogously to $S_P^*$ we define an alternative parallel efficiency $E_P^*$:

$$E_P^* = \frac{2 \cdot t_{2CPUs}}{P \cdot t_{PCPUs}}; \quad P \geq 2 \tag{19}$$

The numerical investigations were carried out on an IBM p575 system with 32 IBM Power6 Cores (4.7 GHz) per node. Figure 8 a) shows the computing times for both domain sizes

together with the linear speedup for the reference computing times obtained for 1 and 2 CPUs. The very low speedup from 1 to 2 CPUs (compare also figure 8 c) and d)) is remarkable and can be explained by communication latencies as well as the largest interface size (compare figure 7). Further it can be stated that latencies play a big role for the overall parallel efficiency of the presented method, since the simple explicit scheme performs relatively few operations until a data exchange between two CPUs takes place.
Applying the alternative definition of the parallel speedup and the parallel efficiency (equations (17) and (19)) it can be seen that for a wide range of CPU numbers a good parallel efficiency can be obtained for both domain sizes. For the smaller domain size with approximately $2 \times 10^6$ CVs a superlinear speedup (respectively more than 100% parallel efficiency) is obtained from 4 to 32 CPUs. This behavior can be explained by so called cache effects where the CV number per processor becomes small enough so that a significant part of the problem can be stored in the internal CPU cache which is much faster than the RAM.
Another interesting fact is the change of the slope of the curves for 64 CPUs, where more than one node is incorporated in the computation. A further decline of efficiency can be seen for 128 CPUs where 4 nodes are used. For the smaller domain the overall computation time even increases from 64 to 128 CPUs.
In summary it can be stated that the numerical scheme and its implementation show a good parallel scalability, even for large domains and a large number of processors. Further it can be seen that the presented results can only be interpreted correctly with a certain knowledge of the underlying hardware.

### 4.3 Acoustic Fields Obtained on Different Hierarchically Coarsened Grids and Corresponding Computational Times

Two aeroacoustic simulations of the "plate in the turbulent wake of a circular cylinder" (section 3.2) with two different acoustic grids are carried out in order to investigate the efficiency of the hierarchically coarsened grid method outlined in sections 2.4.1 and 2.4.2 and to study the influence of the coarsened acoustic grid on the obtained results. A simulation where CFD and CAA grids are identical and another simulation where the CAA grid is the 1 times coarsened CFD grid were performed. The numerical parameters for both simulations are summarized in table 3. In figure 9 the aeroacoustic pressure

| | CAA grid = CFD grid | 1×coarsened CFD grid |
|---|---|---|
| # CV of CAA grid | 6321408 | 790176 |
| $\Delta t_{CFD}$ $[s]$ | $1.6 \times 10^{-6}$ | $1.6 \times 10^{-6}$ |
| $\#\Delta t_{CAA}$ within 1 CFD step | 160 | 80 |
| $\Delta t_{CAA}$ $[s]$ | $1.0 \times 10^{-8}$ | $2.0 \times 10^{-8}$ |

Table 3: Numerical parameters for the aeroacoustic simulations.

fluctuation $p'$ is shown for different time steps and the two CAA grids. The computa-

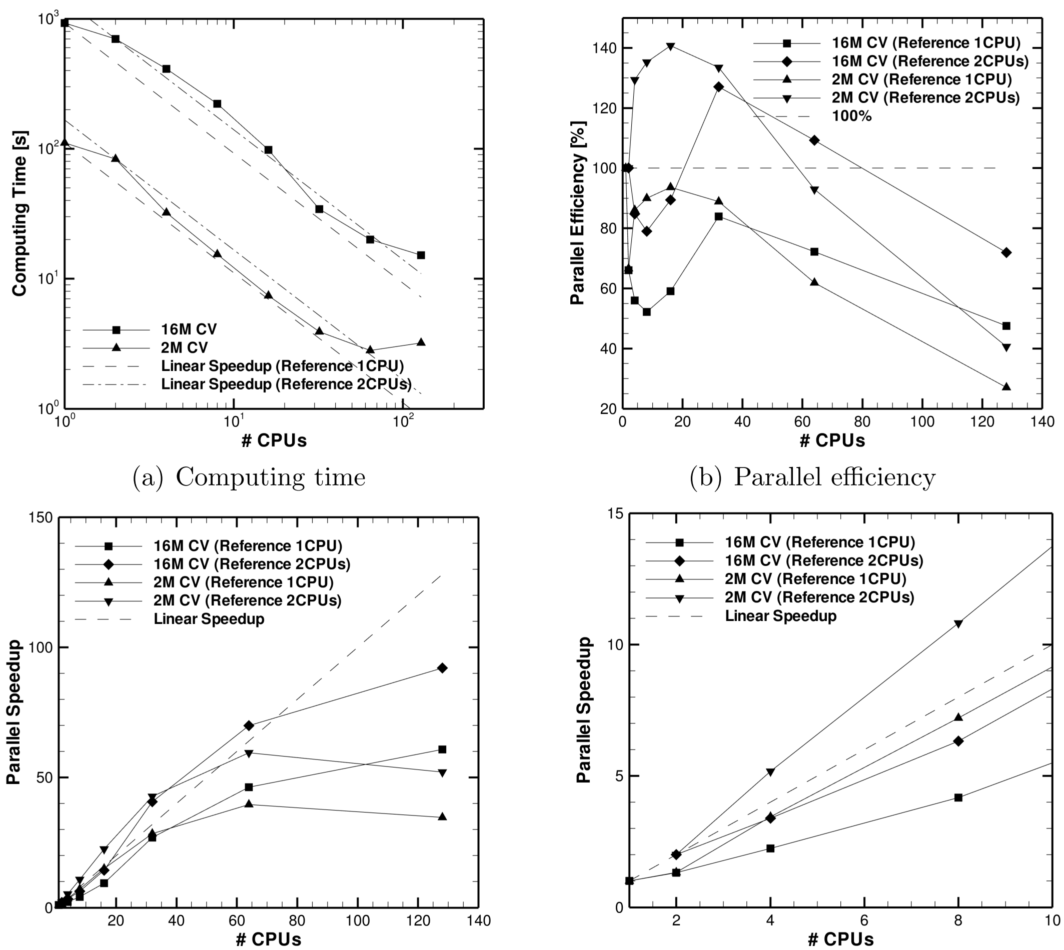


(a) Computing time



(b) Parallel efficiency



(c) Parallel speedup



(d) Parallel speedup - detailed view

Figure 8: Parallel efficiency of the acoustic solver.

tion of the acoustic field was started from the same fully developed turbulent flow field. The results for both simulations with different acoustic grids are in qualitatively good agreement, whereas there are visible differences caused by the dissipative nature of the numerical scheme. Figure 10 shows the computed sound pressure spectra in two monitoring positions MP1 and MP2 ($80mm$ above/below the center of the cylinder). Both spectra for the acoustics on the CFD grid and acoustics on the 1 times coarsened CFD grid are in good agreement for lower frequencies, whereas for higher frequencies, that correspond with shorter wave lengths and therefore a lower resolution, the differences become larger. Nevertheless for many applications the differences in the spectra are acceptable, especially if the focus lies on the qualitative behavior of different configurations during the design process. The computational times for both numerical setups are summarized in figure 11 in comparison to a pure CFD calculation. The differences in the computational times are enormous. The aeroacoustic simulation where the acoustics are computed on

the CFD mesh takes approximately 5 times longer than the simulation with the acoustics on the 1 times coarsened CFD grid. The coupled aeroacoustic simulation with the coarser acoustic grid takes approximately 2 times longer than a pure CFD calculation of the same test case. It can be stated that an enormous benefit in terms of computing time can be achieved applying the described hierarchical grid method.
It should be mentioned that the differences between pure CFD and coupled simulations, as well as between the coupled simulations with different acoustic grids, strongly depend on the convergence behavior of the CFD simulation. For the presented simulation only 4 SIMPLE iterations were necessary to fulfill the convergence criterion. The differences between the simulations would be smaller for a worse convergence behavior since the computing time required for the acoustics stays constant for a given grid with the implemented explicit scheme.

## 5 CONCLUSIONS

We presented a numerical scheme for the simulation of aerodynamic noise caused by flows at low Mach numbers within and/or around complex geometries.
The in-house finite volume flow solver FASTEST [1] was extended by a fully parallelized high resolution finite volume scheme for the linearized Euler equations. To speed up the coupled simulations, a frozen fluid approach as well as a hierarchical grid based method for the aeroacoustic simulation were implemented. To evaluate the numerical and the parallel efficiency of the implemented CAA method, simulations of a generic acoustic test case have been carried out for different domain sizes as well as for different numbers of processors. The implemented scheme shows a good numerical scalability up to a large number of control volumes as well as a good parallel efficiency and a good parallel scalability.
Further coupled aeroacoustic simulations for a “plate in the turbulent wake of a circular cylinder” with different CAA grids have been carried out. The results for different acoustic grids are in qualitatively good agreement. The simulation of the acoustics on the 1 times coarsened CFD grid leads to a speed up of factor 5, compared to the coupled simulation where the acoustics are computed on the CFD grid. The implemented scheme seems to be a very promising approach, especially for situations where the CFD and CAA domain are approximately of the same size. This should be evaluated in further investigations.

## ACKNOWLEDGMENT

This work was partially supported by the Deutsche Forschungsgemeinschaft (DFG) within the collaborative research center “Flow and Combustion in future Gas Turbine Combustion Chambers” (SFB 568).

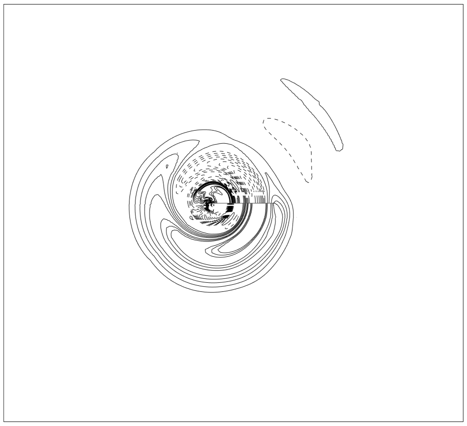

(a) Acoustic pressure $p'$ on CFD grid after 500 $\Delta t_{CFD}$

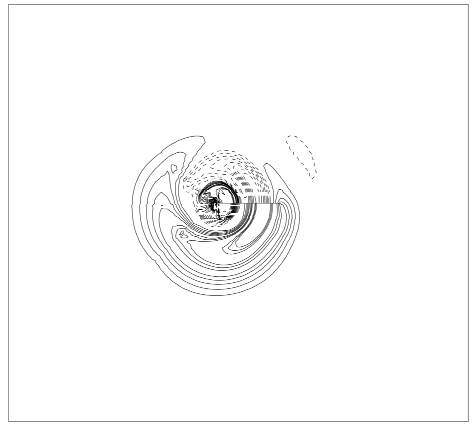

(b) Acoustic pressure $p'$ on $1\times$coarsened CFD grid after 500 $\Delta t_{CFD}$

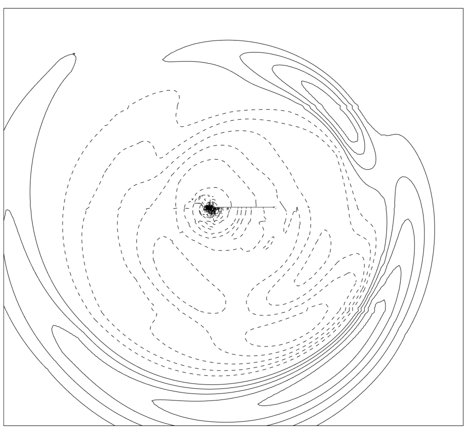

(c) Acoustic pressure $p'$ on CFD grid after 1000 $\Delta t_{CFD}$

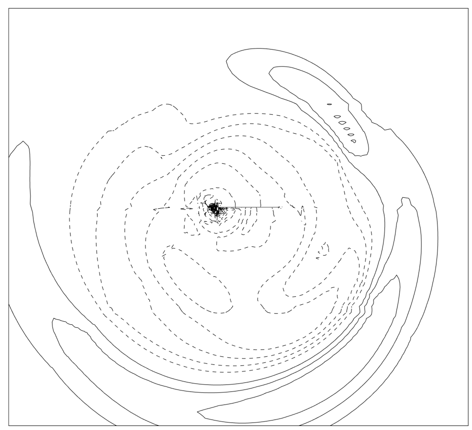

(d) Acoustic pressure $p'$ on $1\times$coarsened CFD grid after 1000 $\Delta t_{CFD}$

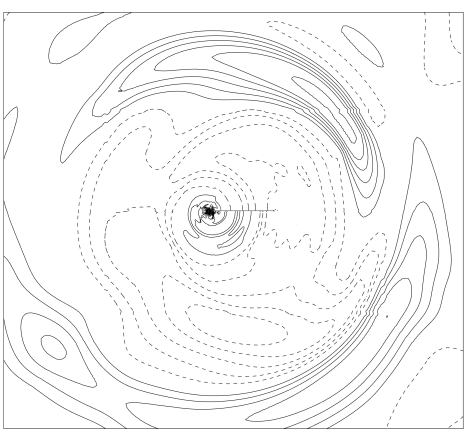

(e) Acoustic pressure $p'$ on CFD grid after 3000 $\Delta t_{CFD}$

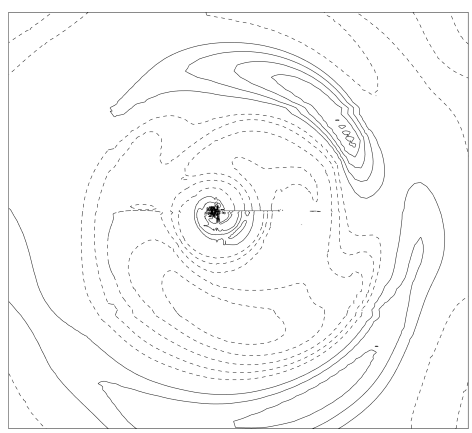

(f) Acoustic pressure $p'$ on $1\times$coarsened CFD grid after 3000 $\Delta t_{CFD}$

Figure 9: Aeroacoustic pressure fluctuation $p'$ obtained for different CAA grids and different time steps after starting the computation of the acoustic field. Levels reach from $-0.03Pa$ to $0.03Pa$. Negative values are plotted with dashed lines.

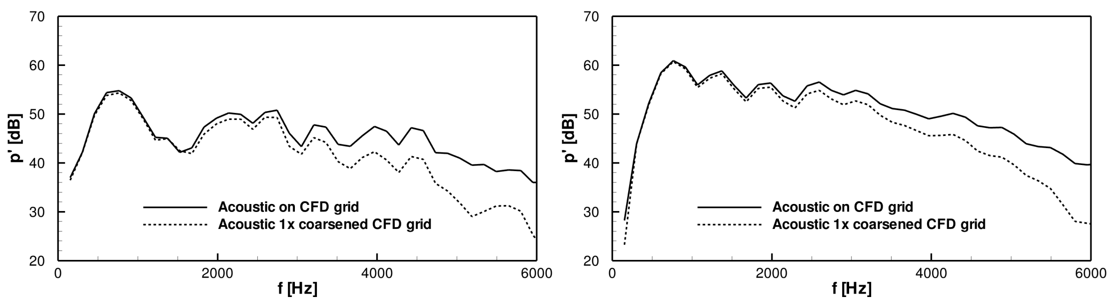


(a) MP1 (b) MP2

Figure 10: Computed sound pressure spectra for two different monitoring positions (MP) and different acoustic grids.

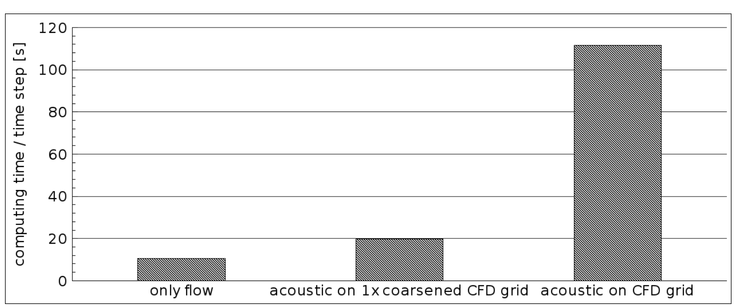


Figure 11: Computing times for one time step and different acoustic grids in comparison to a pure CFD computation.

## REFERENCES

[1] FASTEST-Manual. Technische Universität Darmstadt, Institute of Numerical Methods in Mechanical Engineering. Darmstadt (2005)

[2] J.C. Hardin, D.S. Pope: An Acoustic/Visous Splitting Technique for Computational Aeroacoustics. Theoret. Comp. Fluid Dynamics **6**, 323-340 (1994)

[3] W.L. Briggs, H. Van Emden, S.F. McCormick: A Multigrid Tutorial. SIAM, Philadelphia 2000

[4] M.J. Lighthill: On Sound Generated Aerodynamically 1: General Theory. Proc. Roy. Soc. London Series A **211**, 564-587 (1952)

[5] E.F. Toro: Riemann Solvers and Numerical Methods for Fluid Dynamics. Springer Berlin (1999)

[6] R.J. LeVeque: Finite-Volume Methods for Hyperbolic Problems. Cambridge University Press (2004)

[7] B. Van Leer: Towards the ultimate conservative difference scheme III. Upstream-centered finite-difference schemes for ideal compressible flow. J. Comp. Phys., 23, 263-75 (1977)

[8] M. Kornhaas, M. Winkler, D.C. Sternel, K. Becker, M. Schäfer and F. Kameier: LES of cylinder plate configurations and corresponding aeroacoustic effects. Proc. of 19ième Congrès Français de Mécanique, August 24-28 2009, Marseille, France

[9] M. Germano, U. Piomelli, P. Moin, W.H. Cabot: A dynamic subgrid-scale eddy viscosity model. Phys. of Fluids A **3(7)**, 1760-1765 (1991)